

Technical note: Evaluation of an x-ray imaging system during the image acquisition stage using high frequency residuals of line profiles

Antonio González-López

Hospital Universitario Virgen de la Arrixaca, ctra. Madrid-Cartagena, 30120 El Palmar (Murcia), Spain

Version typeset May 17, 2022

Author to whom correspondence should be addressed. email:
antonio.gonzalez7@carm.es

Abstract

Purpose: In this work, the image of a radio-opaque edge is used to investigate the detectability performance of an x-ray imaging system during the image data acquisition stage.

Methods: Several profiles of the edge image are differentiated to create impulse-like signals. Then, high frequency residuals (HFR) of these signals are obtained by removing their first harmonics and detectability is determined for these HFRs using an ideal Bayesian observer. After that, areas under the ROC curves (AUC) are presented as a function of the lowest frequency component remaining in the HFR signal. Two radiation beam qualities and four dose levels are used to obtain the images studied in this work.

Results: The method presented produces plots of AUC versus frequency that clearly distinguish between different doses and beam qualities.

Conclusions: The HFRs generated from an edge image make up a set of decreasing-contrast signals that are suitable for studying in depth the detectability of an imaging system. In addition, given the large number of profiles that can be extracted from the edge image, the uncertainties of the AUC curves are small even when only one image per beam quality and dose is used.

I. Introduction

Quality controls of x-ray imaging devices are carried out as part of system acceptance and commissioning and of periodical quality assurance programs^{1,2}. They are intended to guarantee an optimized performance in both image quality and dose^{3,4,5}.

Image quality has been traditionally associated to some physical parameters of the imaging sensor such as spatial resolution and noise level^{6,7}. Nowadays, image quality assessment in terms of detectability is becoming more and more frequent and new task-based tests are appearing^{8,9,10,11}. The purpose of these tests is to determine the clinical performance of the imaging system, in such a way that the evaluation results are more consistent with its diagnostic capabilities.

According to Tapiovaara and Wagner¹² one of the fundamental imaging stages (image data acquisition) can be analyzed rigorously by using the concept of the ideal observer. In this way, the intrinsic detectability capabilities of the detector can be evaluated without the human observer intervention.

In this work, image data acquisition is analyzed for an x-ray imaging system using beams with different qualities and using different dose levels. For the analysis, images of an edge phantom are used to obtain different test signals on which detectability is evaluated. These test signals are the output of linear transformations of the image and can be seen as high frequency residuals of line profiles calculated as the derivatives of edge profiles on the edge image.

II. Material and methods

The x ray beam was generated in an Ysio Max X-ray system from Siemens. The beam qualities used were RQA 3 and RQA 5. Source-detector distance was set to 153 cm and the field size was set to 15.8 cm \times 15.4 cm.

For each radiation quality two entrance air KERMA were used, 1.79 and 17.9 μ Gy for RQA 3 and 1.76 and 17.6 μ Gy for RQA 5. The imaging detector was a PIXIU 3543 pR from Trixell (CsI coupled to TFT matrix of aSi with a pixel spacing of 0.144 mm \times 0.144 mm).

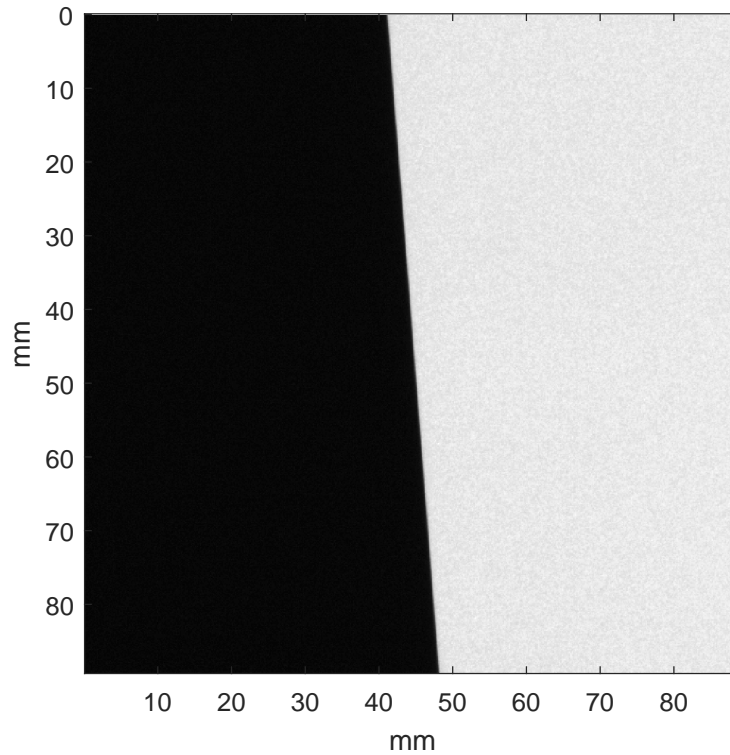


Figure 1: Central part of an image of the edge phantom.

The edge phantom was a TX5 (Scanditronix-Welhöfer). It has a tungsten edge 1 mm thick and 100 mm length. A central part of the image of 90 mm \times 90 mm was used for calculation (figure 1).

Figure 2 shows two parts of the profile resulting from scanning the edge image in figure 1 along its topmost row. Figure 2(a) show the central part of this profile and figure 2(b) shows the rightmost part of it. Signals to detect are obtained from their numerical derivatives (figure 3(a) shows the signal and figure 3(b) shows the absence of signal).

II.A. Test signals

The signals used to assess detectability are obtained as high frequency residuals (HFR) of the output signals shown in figure 3 and their corresponding input signals. Signal in figure 3(a) is the system output $o(x)$ for a delta input $i(x)$ and signal in figure 3(b) is noise or the system output $n_o(x)$ to the absence of signal $n_i(x) \equiv 0$.

High frequency residuals of order k , $r_i^k(x)$, $r_o^k(x)$, $n_i^k(x)$ and $n_o^k(x)$ with $k = 1, 2, ..$ for signals $i(x)$, $o(x)$, $n_i(x)$ and $n_o(x)$ respectively are obtained in a three-step process. First, the

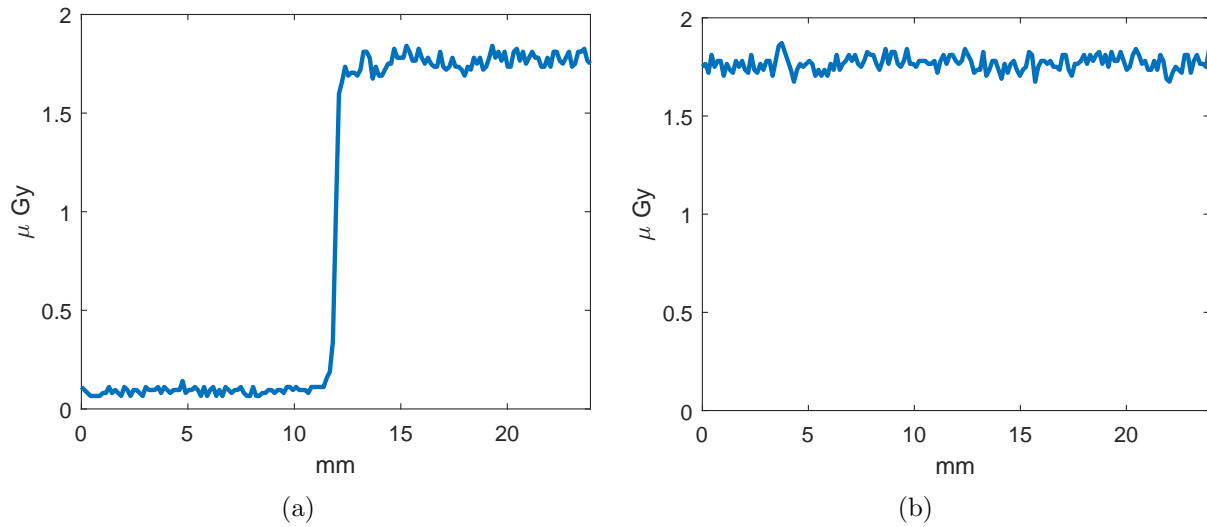


Figure 2: Central (a) and right (b) parts of the uppermost horizontal profile of the edge image in figure 1.

discrete Fourier transform (DFT) of the signal is calculated. Second all Fourier coefficients of order less than k are made zero. Finally, the inverse transform is applied to the processed coefficients to obtain the residual. In this way, the lowest frequency component remaining in the residual of order k corresponds to a frequency

$$f_k = \frac{k}{N\Delta}, \quad (1)$$

where N is the number of points in $i(x)$ and $o(x)$ and Δ is the pixel spacing in the image.

Figure 4 shows the central part of high frequency residuals (orders $k = 1$, $k = 30$ and $k = 60$ from left to right) for the delta input $i(x)$ (thin lines), for the output signal $o(x)$ (upper row and thick lines) and for the noise profile $n_o(x)$ (lower row and thick lines). The interest from the detectability point of view is that, as the order of the HFR increases, the contrast and the low frequency contents of the residual are reduced. Both effects make that signal $r_i^k(x)$ is harder to detect as k increases.

II.B. Derivation of the decision function

According to statistical decision theory, for a digital image the decision function L for an ideal Bayesian observer, expressing the likelihood of an object being present in an image is expressed as the product of the matrices^{13,14}

$$L = f^t H^t C_n^{-1} g, \quad (2)$$

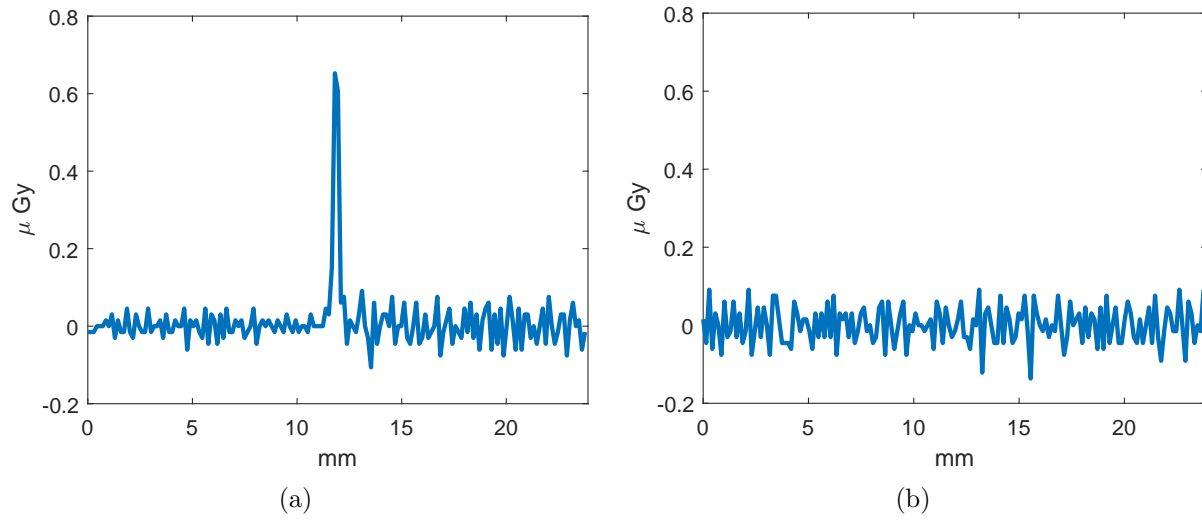


Figure 3: (a) Numerical derivative of profile in figure 2(a). This is the system output $o(x)$ to a delta input. (b) Numerical derivative of profile in figure 2(b). This is noise or the system output $n_o(x)$ to the absence of input signal.

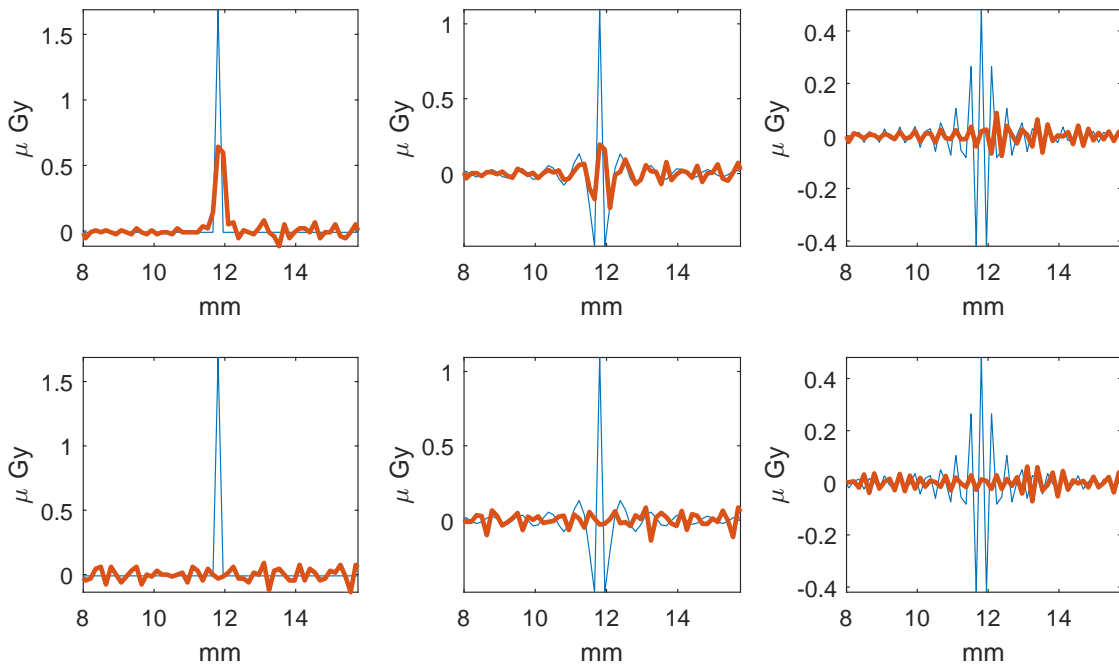


Figure 4: High frequency residuals of orders $k = 1$, $k = 30$ and $k = 60$ for a delta input $i(x)$ (thin lines), for profile $o(x)$ in figure 3(a) (thick lines upper row) and for profile $n_o(x)$ in figure 3(b) (thick lines lower row).

where f is the imaged object, the superscript t stands for the transpose of a matrix, H is the linear system transfer function, C_n is the covariance matrix of noise and g is the image.

By inserting the identity matrix $I = W^*W$ in equation 2, where W is the matrix defining the unitary DFT with matrix elements

$$W_{k,l} = \frac{e^{-i2\pi kl/N}}{\sqrt{N}}, \quad k, l = 0, \dots, N-1, \quad (3)$$

N is the length of the signals and the asterisk denotes the matrix with complex conjugated entries (not the Hermitian matrix), L can be rewritten as

$$L = f^t H^t W^* W C_n^{-1} g. \quad (4)$$

Now, since for a shift invariant system the matrix H is a circulant matrix, its autovectors are the columns of W and its autovalues are the components of the system OTF \hat{h} (the DFT of the first row h of H), we have

$$HW = W \text{diag}(\hat{h}), \quad (5)$$

where $\text{diag}(v)$ is the diagonal matrix in which the diagonal elements are the elements of vector v . Using this result and assuming that H is real and symmetric the term $H^t W^*$ in equation 4 can be written as

$$H^t W^* = HW^* = (HW)^* = (W \text{diag}(\hat{h}))^* = W^* \text{diag}(\hat{h}^*). \quad (6)$$

In this way, since $f^t W^* = \hat{f}^{*t}$ equation 4 can be written as

$$L = \hat{f}^{*t} \text{diag}(\hat{h}^*) W C_n^{-1} g. \quad (7)$$

Since covariance matrices C_n are real, symmetric and circulant, $C_n W = W \text{diag}(\hat{c})$, with \hat{c} being the DFT of the first row of C_n and its absolute value the noise power spectrum (NPS), we have

$$C_n = W^* W C_n = W^* (W \text{diag}(\hat{c}))^t = W^* \text{diag}(\hat{c}) W \quad (8)$$

and

$$C_n^{-1} = W^* \text{diag}(\hat{c})^{-1} W. \quad (9)$$

Therefore, equation 2 can be written as a product of the Fourier transforms of the terms in equation 2

$$L = \hat{f}^{t*} \text{diag}(\hat{h}^*) \text{diag}(\hat{c})^{-1} \hat{g}, \quad (10)$$

that is,

$$L = \sum_{l=0}^{N-1} \frac{\hat{f}_l^* \hat{h}_l^* \hat{g}_l}{\hat{c}_l}. \quad (11)$$

For real symmetric point spread function and object, \hat{f}^* and \hat{h}^* will also be real and symmetric. In addition, since c is a real and symmetric, \hat{c}^* will also be real and symmetric. In the case of g , because of noise it will only be approximately symmetric, however, in average it will be. For these reasons, the terms in equation 11 will be substituted by their absolute values. In this way the alignment of the different Fourier transformed functions will also be guaranteed as taking absolute values is equivalent to selecting the origin of frequencies at the axis of symmetry of the functions. Therefore, as $|\hat{h}_l^*| = MTF_l$ and $|\hat{c}_l| = NPS_l$ we have

$$L \approx \sum_{l=0}^{N-1} \frac{|f_l| MTF_l |\hat{g}_l|}{NPS_l}. \quad (12)$$

Then, decision function values for each residual $r_i^k(l)$ are obtained for the IBO observer on the signal-present profile as,

$$L_{sp}^k = \sum_{l=0}^{N-1} \frac{|\hat{r}_i^k(l)| MTF(l) |\hat{r}_o^k(l)|}{NPS(l)} \quad (13)$$

and on the signal-absent profile,

$$L_{sa}^k = \sum_{l=0}^{N-1} \frac{|\hat{r}_i^k(l)| MTF(l) |\hat{n}_o^k(l)|}{NPS(l)} \quad (14)$$

where $\hat{r}_i^k(l)$ is the DFT of the residual of the delta input, $\hat{n}_i^k(l) \equiv 0$ is the DFT of the residual of the input profile for noise, OTF is the optical transfer function of the system, W_n is the DFT of the noise autocovariance, its absolute value being the noise power spectrum, and $\tilde{r}_o^k(l)$ and $\tilde{n}_o^k(l)$ are the DFTs of the residuals of the line profiles.

From image in figure 1, a total of $N_{prof} = 625$ horizontal profiles can be extracted. Therefore, 625 values of the decision function for signal-present and the same number for signal-absent can be calculated for each order k .

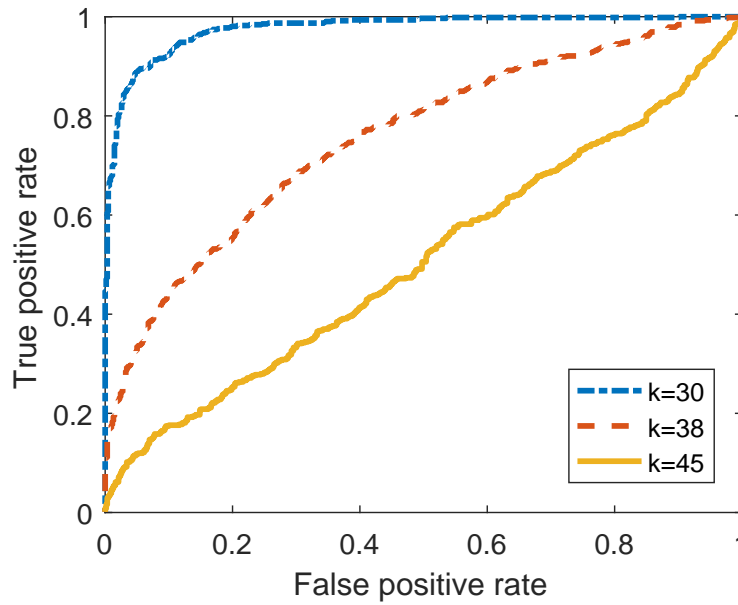


Figure 5: ROC curves for residuals of orders $k = 30$, $k = 38$ and $k = 45$. The RQA 3 image acquired with $1.79 \mu Gy$ of entrance air KERMA was used.

III. Results

Figure 5 shows three examples of the ROC curves used to produce an AUC curve. These curves corresponds to residuals $k = 30$, $k = 38$ and $k = 45$ of the topmost profile in the RQA 3 image acquired with $1.79 \mu Gy$ of entrance air KERMA. These residuals correspond to frequencies $f_{30} = 1.25 \text{ mm}^{-1}$, $f_{38} = 1.59 \text{ mm}^{-1}$ and $f_{45} = 1.88 \text{ mm}^{-1}$ respectively ($N = 166$ in equation 1 for profiles of 24 mm length).

Figure 6 shows the results obtained in this work on detectability of the imaging system for the different beam qualities and the different entrance air KERMA. The area under the ROC curve is plotted versus the frequency f_k of the lowest frequency component in residual r_i^k . It can be seen the large effect that dose has on detectability. For both beam qualities, increasing the dose by a factor of 10 makes the AUC rise from 0.5 to 1 in a frequency interval with a length of about 0.5 mm^{-1} . This means that, in that interval, HFR signals go from absolutely undetectable to absolutely detectable. Such differences do not happen between the different beam qualities. In particular, for the highest doses both beam qualities show a similar detectability.

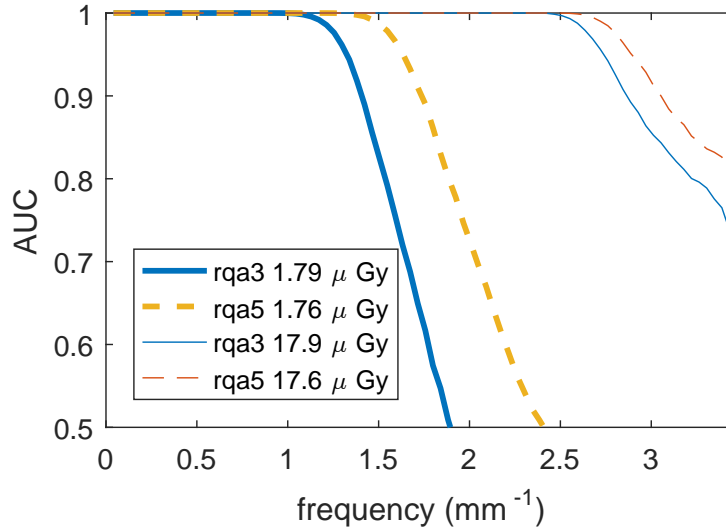


Figure 6: Area under the ROC curve versus f_k for the different beam qualities and entrance air KERMA's used in this work.

IV. Discussion

Figure 6 shows that the higher beam quality RQA 5 gives better detectability results than the lower RQA 3. This should not be strange since detectability of an object in an image depends on the physical properties of the imaging system like noise and spatial resolution, some characteristics of the object such as its shape, size and contrast and on the decision function of the observer model used^{13,15}. In this way, the results presented in this work for detectability are obtained for the high-frequency residuals of a delta wave obtained from an object that produces an image with extremely high contrast. How much these signals represent other signals is a question not easy to answer. In an ideal digital lineal system, responses to digital delta waves conform a base for output signals, meaning that any other output signal can be uniquely obtained as a linear combination of them. It's worth noting that the decision function for an IBO observer is linear in the data^{13,14}.

Figure 5 shows how detectability drops drastically between $f_{30} = 1.25 \text{ mm}^{-1}$ and $f_{45} = 1.88 \text{ mm}^{-1}$. This frequency range can be used to characterize detectability of the imaging system for the given beam quality and entrance air KERMA. Similar information can be extracted in a quicker and more precise way from figure 6 for the different combinations of beam qualities and entrance air KERMA. For instance, for the highest doses, detectability starts worsening at frequencies 2.5 and 2.7 mm^{-1} for RQA 3 and RQA 5 beam qualities respectively.

V. Conclusion

In this work, statistical decision theory has been applied to determine performance of an x-ray imaging system in terms of detectability at the image data acquisition stage. This intrinsic characteristic of the imaging system has been studied for different beam qualities and different doses, and for each combinations of them one only image of an edge phantom has been used.

The set of signals to be detected is built from a delta input and the signals are obtained by eliminating the lowest frequency components of the delta. The resulting high frequency residuals make up a series of signals in which contrast decreases as the order of the residual increases. At the same time, the frequency band of the residuals is shifted to higher frequencies. The fact that both effects make detectability of the residual more difficult can be exploited to determine the limits of system performance.

The final result of this procedure presents the AUC value for each residual versus the lowest limit of its frequency content. In this way, the frequency interval in which the curve drops from 1 to 0.5 characterizes the performance limits of the system in terms of detectability, for a given beam quality and a given entrance air KERMA and for the conditions in which the test is carried out.

References

- ¹ E. Samei, L. C. Ikejimba, B. P. Harrawood, J. Rong, I. A. Cunningham, and M. J. Flynn, Report of AAPM Task Group 162: Software for planar image quality metrology, *Medical Physics* **45**, e32–e39 (2018).
- ² N. W. Marshall, A. Mackenzie, and I. D. Honey, Quality control measurements for digital x-ray detectors, *Physics in Medicine and Biology* **56**, 979–999 (2011).
- ³ H. Yan, L. Cervino, X. Jia, and S. B. Jiang, A comprehensive study on the relationship between the image quality and imaging dose in low-dose cone beam CT, *Physics in Medicine and Biology* **57**, 2063–2080 (2012).

-
- ⁴ P.-J. P. Lin, B. A. Schueler, S. Balter, K. J. Strauss, K. A. Wunderle, M. T. LaFrance, D.-S. Kim, R. H. Behrman, S. J. Shepard, and I. H. Bercha, Accuracy and calibration of integrated radiation output indicators in diagnostic radiology: A report of the AAPM Imaging Physics Committee Task Group 190, *Medical Physics* **42**, 6815–6829 (2015).
- ⁵ J. S. Jang, H. J. Yang, H. J. Koo, S. H. Kim, C. R. Park, S. H. Yoon, S. Y. Shin, and K.-H. Do, Image quality assessment with dose reduction using high kVp and additional filtration for abdominal digital radiography, *Physica medica* **50**, 46–51 (2018).
- ⁶ C. J. Strudley, K. C. Young, P. Looney, and F. J. Gilbert, Development and experience of quality control methods for digital breast tomosynthesis systems, *The British Journal of Radiology* **88**, 20150324 (2015).
- ⁷ J. Solomon, J. Wilson, and E. Samei, Characteristic image quality of a third generation dual-source MDCT scanner: Noise, resolution, and detectability, *Medical Physics* **42**, 4941–4953 (2015).
- ⁸ E. Samei, D. Bakalyar, K. L. Boedeker, S. Brady, J. Fan, S. Leng, K. J. Myers, L. M. Popescu, J. C. Ramirez Giraldo, F. Ranallo, J. Solomon, J. Vaishnav, and J. Wang, Performance evaluation of computed tomography systems: Summary of AAPM Task Group 233, *Medical Physics* **46**, e735–e756 (2019).
- ⁹ I. Hernandez-Giron, A. Calzado, J. Geleijns, R. M. S. Joemai, and W. J. H. Veldkamp, Low contrast detectability performance of model observers based on CT phantom images: kVp influence, *Physica medica* **31**, 798–807 (2015).
- ¹⁰ B. L. Eck, R. Fahmi, K. M. Brown, S. Zabic, N. Raihani, J. Miao, and D. L. Wilson, Computational and human observer image quality evaluation of low dose, knowledge-based CT iterative reconstruction, *Medical Physics* **42**, 6098–6111 (2015).
- ¹¹ N. V. Peteghem, H. Bosmans, and N. W. Marshall, NPWE model observer as a validated alternative for contrast detail analysis of digital detectors in general radiography, *Physics in Medicine and Biology* **61**, N575–N591 (2016).
- ¹² M. J. Tapiovaara and R. F. Wagner, SNR and noise measurements for medical imaging: I. A practical approach based on statistical decision theory, *Physics in Medicine and Biology* **38**, 71–92 (1993).
-

-
- ¹³ ICRU, ICRU Report 54: Medical Imaging-The Assessment of Image Quality, Technical report, 1995.
- ¹⁴ K. Fukunaga, *Introduction to Statistical Pattern Recognition*, Elsevier, 1990.
- ¹⁵ G. J. Gang, J. W. Stayman, W. Zbijewski, and J. H. Siewerdsen, Task-based detectability in CT image reconstruction by filtered backprojection and penalized likelihood estimation, *Medical Physics* **41**, 081902 (2014).